Experimental Thermal and Fluid Science 40 (2012) 81–92

Contents lists available at SciVerse ScienceDirect

Experimental Thermal and Fluid Science

journal homepage: www.elsevier.com/locate/etfs

Macroscopic characteristics for direct-injection multi-hole sprays using dimensionless analysis

Wei Zeng [a], Min Xu [a,*], Ming Zhang [a], Yuyin Zhang [a], David J. Cleary [b]

[a] School of Mechanical Engineering, Shanghai Jiao Tong University, National Engineering Laboratory for Automotive Electronic Control Technology, Shanghai 200240, China
[b] General Motors Global Research & Development, China Science Lab, Shanghai 201206, China

ARTICLE INFO

Article history:
Received 9 May 2011
Received in revised form 1 February 2012
Accepted 10 February 2012
Available online 7 March 2012

Keywords:
Direct-injection multi-hole spray
Macroscopic characteristics
Weber number
Reynolds number
Air-to-liquid density ratio
Dimensionless correlations

ABSTRACT

The macroscopic spray characteristics were quantified using dimensionless analysis by examining the role of the dominating forces associated with liquid-jet breakup. The Weber number, Reynolds number, and air-to-liquid density ratio dimensionless numbers were used to capture the primary forces including the inertia, viscous, surface tension, and aerodynamic drag forces. Planar Mie-scattering technique was applied to generate spray images over a broad range of conditions found in today's spark-ignition-direct-injection (SIDI) engines, providing a relatively large range of dimensionless numbers. The effect of fuel properties were examined using gasoline, methanol and ethanol fluids. Six regions described on a Weber number versus Reynolds number domain were selected to identify the relative importance of the inertia force, surface tension force, and viscous force on macroscopic spray structure. The effect of aerodynamic drag was individually determined by characterizing the spray over a range of ambient air-to-liquid density ratios. As a result, for the non-flash-boiling multi-hole sprays in this study, the Weber number and air-to-liquid density ratio have much more profound effect on the spray penetration and spray–plume angle compared to the Reynolds number contribution. The inertia force and air drag force are more important factors compared to the viscous force and surface tension force. This analysis yielded dimensionless correlations for spray penetration and spray–plume angle that provided important insight into the spray breakup and atomization processes.

1. Introduction

Macroscopic spray characteristics, such as spray penetration, spray–plume angle and droplet size distribution are critical parameters that influence the in-cylinder air–fuel mixture and combustion process of the internal combustion engine. The spray performance is influenced by a large number of parameters, including the fuel pressure, fuel temperature, ambient pressure, ambient temperature, fuel properties, and nozzle geometry [1]. A number of previous studies have investigated these parameters and the corresponding effect on macroscopic spray structure [2–8]. For example, Hiroyasu [2,3] has investigated both the macroscopic and microscopic spray characteristics of the diesel spray under various conditions, providing a set of empirical formulations that describes the spray penetration, spray–plume angle, and Sauter-Mean-Diameter (SMD). More recently, Naber and Siebers [9] and Desantes et al. [10,11] suggested the models for spray penetration based on the characterization of diesel spray and some classical atomization theories. However, these formulations were based on diesel sprays that may not be directly applicable to gasoline and increasingly used gasoline substitutes, such as methanol and ethanol. Zigan et al. [12,13] investigated the fuel effects on spray characteristics and the results indicate that the internal nozzle flow, the injected mass and the spray droplet size distribution is different due to viscosity. Also, Wang et al. [4], Aleiferis et al. [5] and Lee and Reitz [6] characterized sprays for different fuels over various conditions and reported considerable dependence on fuel type and test conditions. These data illustrate the need to establish new and generalized correlations to comprehend the fuel type and test conditions over the operating range of the internal combustion engines.

The primary breakup of the liquid jet into ligaments and droplets represents the initial and critical transition that has significant influence on the spray. The physical process and mechanisms associated with the initial breakup process is known to depend on the competition among the jet inertial force, surface tension force, viscous force, and drag force. Previous studies have used dimensionless numbers to identify the relative importance of these forces [1,14], working toward establishing a better physical description of the jet breakup process. For example, Ohnesorge classified this breakup phenomenon into three regions using the Ohnesorge number and Reynolds number to characterize the transitional rate of droplet formation [1]. Liu and Reitz [15] classified the spray

* Corresponding author.
E-mail address: mxu@sjtu.edu.cn (M. Xu).

0894-1777/$ - see front matter © 2012 Elsevier Inc. All rights reserved.
doi:10.1016/j.expthermflusci.2012.02.003

atomization phenomena into four regions within a Weber number versus Reynolds number domain based on droplet shape. In each region, the dominant forces were identified and the effects of these forces on spray breakup were qualitatively analyzed. The domain was divided into four isolated regions where each region had a unique model. However, correlations that characterize the spray using dimensionless numbers and cover the entire domain have not yet been developed.

This work focuses on the characterization of a multi-hole spray using dimensionless analysis. Weber number, Reynolds number, and air-to-liquid density ratio were used to represent the four primary forces that are known to influence the spray. The planar Mie-scattering technique was implemented to characterize the macroscopic spray structure over a broad range of conditions found in a today's direct-injection engines, providing relatively large ranges of the dimensionless numbers. The effect of fluid property was described in this analysis for gasoline, methanol and ethanol fuels. Correlations relating the spray penetration and spray–plume angle to dimensionless numbers have been generated over the entire domain, providing important insight into the spray breakup and atomization processes. For the experimental conditions used in this study, flash-boiling occurs at the conditions that the ambient pressure is below the saturation pressure. The atomization mechanism of the flash-boiling spray is a different phenomenon compared to that of the non-flashing-boiling sprays and requires a separate analysis [16]. Therefore, the correlations do not apply in the flash-boiling region.

2. Apparatus

Fig. 1 shows the schematic of the experimental apparatus consisting of a constant pressure chamber, a high-pressure fuel supply system, a fluid temperature control system, a chamber pressurization system, a vacuum system and a laser diagnostic system. The injector was installed vertically at the top of the chamber that has an inner diameter of 203 mm and a height of 692 mm. Four quartz windows around the chamber provided full optical access. The chamber ambient pressure was maintained with either the vacuum system or the high-pressure nitrogen filling system. A heat exchanger system was designed to control the fuel temperature over a range of −15 °C to 90 °C. The fuel temperature is managed using a water conditioning system, where a water jacket was designed to surround the injector and an external system conditions the water to reach the desired fuel temperature. An injector with thermal couple was used to correlate the water temperature with the fuel temperature. Three accumulators were used to provide injection pressures up to 10 MPa for gasoline, methanol, and ethanol fluids.

Planar Mie-scattering technique was implemented to characterize the spray. The injected fuel was illuminated by a thin laser sheet of approximately 1 mm generated by a Nd:YAG laser (pulse width: 4 ns, power: 220 mJ at 532 nm). Images of the illuminated spray were captured by a CCD camera (12 bit, 1376 × 1040 resolution, and 15 fps recording rate). A programmable timing unit (PTU) was used to synchronize the laser, the CCD camera, and the injector driver.

The images were post-processed using our recently developed image analysis tool. At each test condition, the background image was recorded and subtracted from the spray images. A threshold value, selected according to the SAE J2715 standard, was used to distinguish between background noise and fuel spray droplets. The in-house developed software was used to produce a histogram of the image intensity for determining the threshold value. Pixel values below this threshold value were set to zero. Spray penetration and spray–plume angle were measured for individual single-shot images. By acquiring 15 images for each test condition at each time-step, averaged data along with statistical variance were generated. More than 150 images were generated and the average value and standard deviation as a function of image number at typical conditions were analyzed. The average value and standard deviation become constants when the image number is above 15 so that 15 images were taken at each condition. The maximum standard deviation for spray penetration is about 2.3 mm, which is observed at a 10 MPa injection pressure condition, see Fig. 10 below.

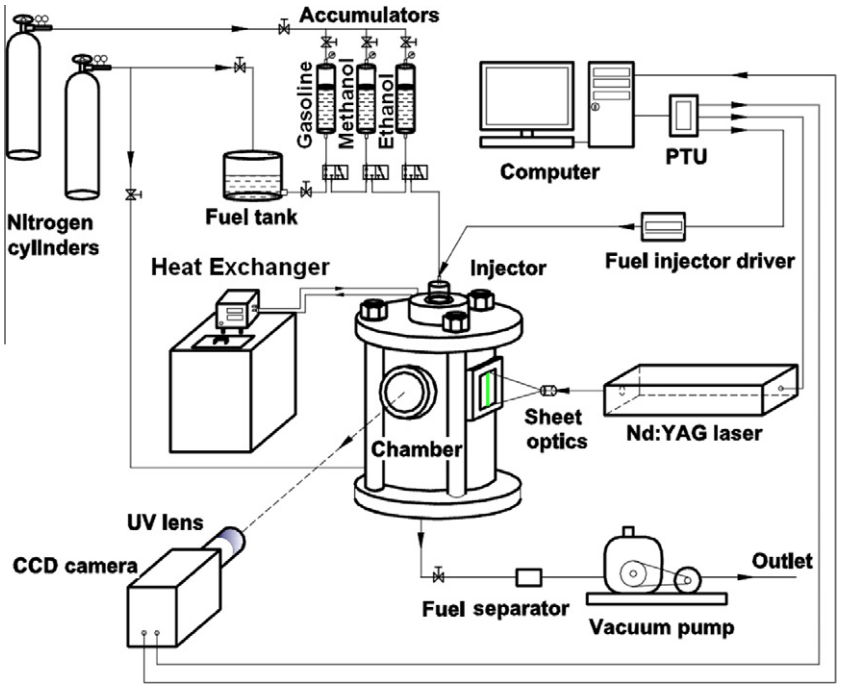

Fig. 1. Schematic of experimental apparatus.

3. Experimental conditions and fuel properties

For today's spark-ignition-direct-injection (SIDI) engines, the fuel is injected into ambient pressures from 20 kPa up to 500 kPa absolute or more, the fuel temperature was varied from −10 °C to over 90 °C, and the injection pressure was varied from 2 MPa to over 10 MPa [5]. Therefore, the experimental conditions used in this study were selected to cover all these engine operating conditions, as summarized in Table 1a. The test fuels were standard commercial grade gasoline (RON 97), analytical grade ethanol and methanol. Table 2 summarizes the physical properties at the atmospheric conditions of these three fuels.

For the test matrix used in this study, flash-boiling occurs at the conditions that the ambient pressure is below the saturation pressure. For reference, Fig. 2 shows the saturation pressure for methanol and ethanol fluids and the typical spray injection and in-cylinder ambient conditions found in SIDI engines. Depending on the specific fuel, this phenomenon will occur at idle, part-load and wide-open-throttle (WOT) operating conditions. At a fuel temperature of 90 °C, for example, flash-boiling occurs for methanol and ethanol fuels at ambient pressures of 260 kPa and 170 kPa, respectively. For these superheated conditions, fuel vapor is generated within the liquid where bubbles undergo an expansion process resulting in a rapid disintegration of the liquid into smaller droplets (namely prompt atomization) [17,18]. The breakup mechanism of the flash-boiling spray is a significantly different phenomenon compared to that of the non-flashing-boiling sprays and requires a separate analysis [16]. Therefore, the data points in the flash-boiling region were not used to yield the correlations for non-flash-boiling sprays, which are shown in Table 1b.

4. Weber and Reynolds numbers dependence

For non-flash-boiling sprays, the breakup process and spray characteristics can be analyzed using Weber number ($We = \rho_l dU^2/\sigma$), Reynolds number ($Re = \rho_l dU/v_l$), and the air-to-liquid density ratio (ρ_a/ρ_l). In these equations, d is the nozzle diameter, ρ_l and ρ_a are the densities of liquid and surrounding air, respectively, U is the jet velocity through the nozzle, σ is the surface tension, and v_l is the viscosity of liquid. These dimensionless parameters ideally comprehend the effects of fluid properties, ambient pressure, fuel pressure, fuel temperature, and nozzle diameter. More specifically, the Weber number represents the ratio of the inertia force to surface tension force, the Reynolds number represents the ratio of the inertia force to the viscous force, and the air-to-fuel density ratio is used to capture the effect of aerodynamic drag force.

Table 1a
Experimental conditions.

Conditions	Values
Injection pressure (MPa)	0.6, 1.1, 3.1, 5.1, 7.1, 10.1
Ambient temperature (°C)	25 ± 1
Back pressure (kPa)	40, 70, 100, 300, 500, 700, 1000
Fuel temperature (°C)	−15, 0, 20, 55, 90

Table 1b
Data points in flash-boiling region.

Fuel	Test conditions (fuel temperature (°C), ambient pressure (kPa))
Gasoline	(55, 40), (55, 70), (90, 40), (90, 70), (90, 100)
Methanol	(55, 40), (55, 70), (90, 40), (90, 70), (90, 100)
Ethanol	(55, 40), (90, 40), (90, 70), (90, 100)

Table 2
Physical properties of test fuels at atmospheric condition.

Test fuel	Gasoline	Methanol	Ethanol
Surface tension (mN/m, 25 °C)	20-25	22.5	22.39
Viscosity (mPa s, 25 °C)	0.42	0.541	1.052
Density (g/mL, 25 °C)	0.740	0.784	0.782
Distillation (T10, T50, T90, T100, (°C))	49.4/84.8/161.2/ 191.8	/	/
Boiling point (°C)	/	64.5	78.3
Heat of vaporization (kJ/kg)	380	1185	920

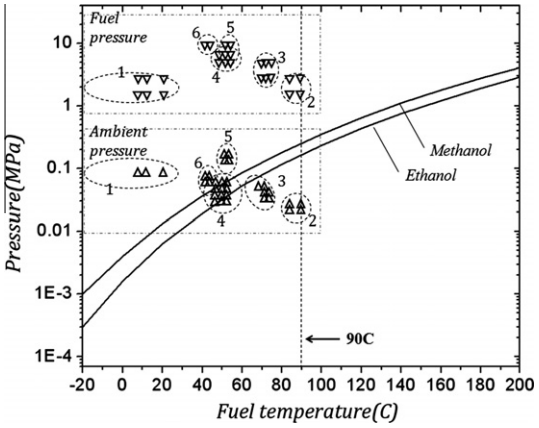

Fig. 2. Typical fuel injection and in-cylinder ambient conditions found in direct-injection engines (regions include cold and warm operation, cold-start (1), idle (2), part-load (3 and 4), and wide-open-throttle (5 and 6) conditions).

Calculation of the Weber and Reynolds numbers requires accurate fuel property values. For this study, the density, viscosity, and surface tension were measured for the tested gasoline, methanol, and ethanol fuels at fuel temperature ranging from −10 °C to 70 °C [19]. The fuel property data for fuel temperatures between 70 °C and 90 °C were extrapolated from the trend lines established in this previous study. As shown in Fig. 3a, the density of these fuels decrease with increasing fuel temperature with similar densities determined for ethanol and methanol fuels. The viscosity has a significant temperature and fuel-type dependence. In particular, ethanol has the largest dependence on temperature for the range shown in Fig. 3b. The viscosity trend for methanol and gasoline are similar, where gasoline has somewhat lower viscosity for this temperature range. A significant difference in viscosity is observed at the lower temperature conditions that diminish with increasing fuel temperature. As shown in Fig. 3c, the surface tension linearly decreases with increasing fuel temperature where marginal differences are observed among these three fuels.

A high-pressure Bosch HEDV 1.2 eight-hole injector with a nozzle diameter of 0.0015 mm and a nominal spray angle of 60° was used. The jet velocity through the nozzle was calculated using Bernoulli's equation, as shown in expression (1). In expression (1), C_D is the discharge co-efficient. ΔP is the difference between injection pressure and ambient pressure. ρ_L is the liquid density.

$$U = C_D \times \sqrt{2 \times \Delta P/\rho_L} \tag{1}$$

The empirical correlation cited by Ref. [1] was used to provide a prediction for the discharge co-efficient of the injector for non-flash-boiling spray, which is shown as follows:

$$C_D = [1.23 + 58 \times (L/D)/\mathrm{Re}]^{-1} \tag{2}$$

where C_D is the discharge co-efficient and Re is Reynolds number. L/D is the nozzle length to diameter ratio and this number is 2 for the nozzle used in this study. According to Asihmin' study, for L/D in the

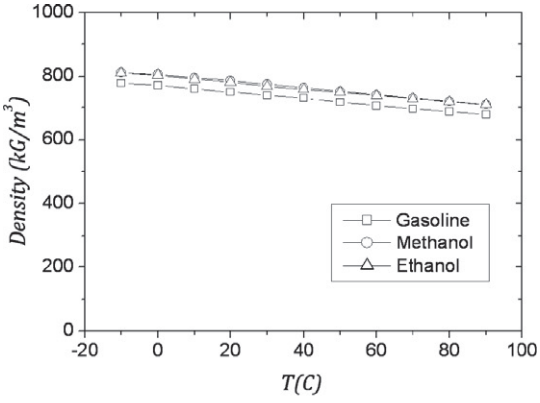

(a) Density

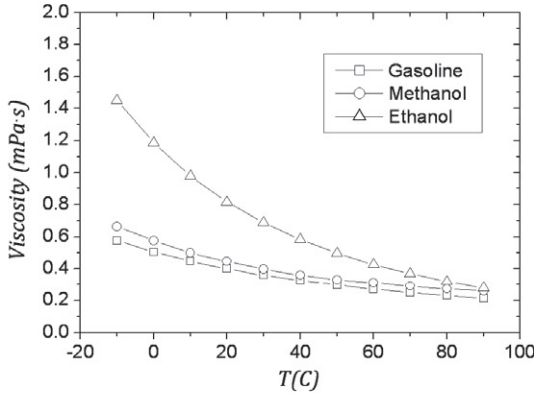

(b) Viscosity

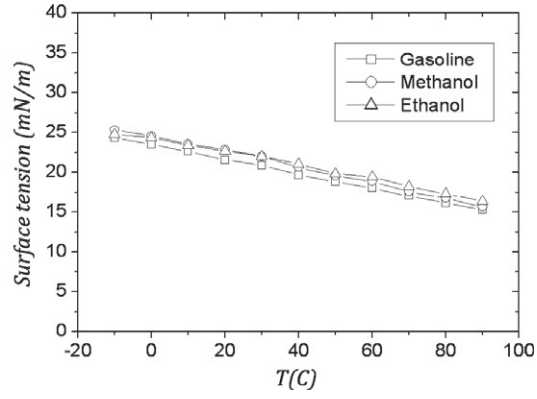

(c) Surface tension

Fig. 3. Density, viscosity and surface tension of test fuels [13].

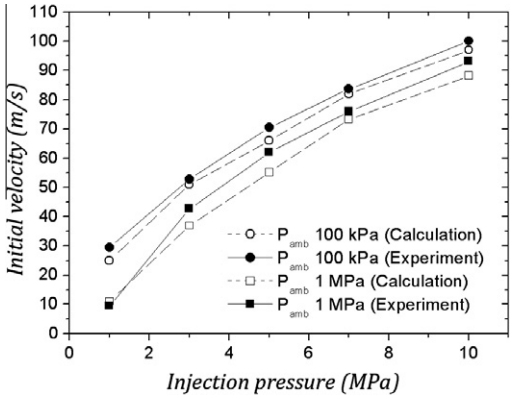

Fig. 4. Discharge co-efficient under different conditions.

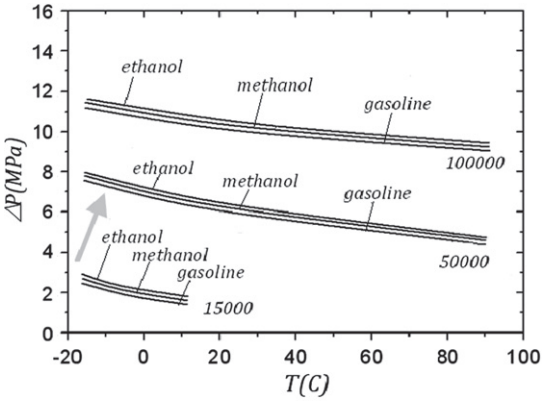

(a) Weber number

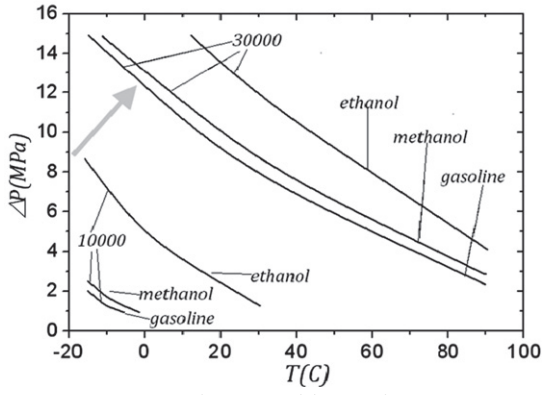

(b) Reynolds number

Fig. 5. Effect of fuel properties, injection and ambient conditions on Weber number and Reynolds number.

range 2–5 and Reynolds number in the range 100–1.5×10^5, the accuracy is high.

In this study, the value of *L/D* is 2 and the Reynolds number ranges from 2000 to 60,000. The predicted results of initial velocity for gasoline are shown in Fig. 4. On the other hand, jet velocity through the nozzle also estimated from the spray penetration data derived from sequential spray images. Fig. 4 provides the comparison between these two velocities under different conditions at 1 ms after the start-of-injection. At this timing, the injector is at full needle lift. The injection duration of all these conditions is 1.5 ms. It can be observed that although there is a small deviation the calculated jet velocity agrees with the results derived from sequential spray images. According to Refs. [20–22], cavitation likely occurs at some test conditions in this study and it results in the uncertainty of expression (2). The effect of flash-boiling on discharge co-efficient did not be considered here since the data points in the flash-boiling region were not used to yield the correlations.

Fig. 5a illustrates the calculated isometric lines of liquid Weber number for the gasoline, methanol and ethanol sprays over the injection and ambient conditions evaluated in this study. Larger Weber numbers occur with higher nozzle pressure differential and with higher fuel temperature. Also, the Weber number of ethanol is smaller than that of methanol while gasoline has the largest Weber number, but the difference among them is slight. The Weber number is relatively more sensitive to the nozzle pressure

differential, with a smaller dependency on the fuel temperature and fuel type. As described in Fig. 3c, the surface tension at −10 °C is only about 1.5 times larger than the surface tension at 90 °C. However, the inertia force at the injection pressure of 10 MPa is about 20 times larger than the inertia force at 0.5 MPa. The change in surface tension force with fuel temperature is considerable smaller compared to the change in the inertia force associated with fuel pressure. The Weber number, therefore, primarily represents the effect of inertia force with secondary contributions due to fuel type and fuel temperature.

Fig. 5b illustrates the calculated isometric lines of liquid Reynolds number for gasoline, methanol and ethanol sprays over the injection and ambient conditions evaluated. Larger Reynolds numbers occur by increasing the nozzle pressure differential or by increasing the fuel temperature. At a specific fuel pressure, a larger change in Reynolds number is determined for Ethanol due to the more significant viscosity dependence on temperature. The viscosity of ethanol at −15 °C, for example, is about seven times larger than the viscosity of gasoline at 90 °C. These data illustrate that both inertia and viscous forces are important contributors to the Reynolds number trends described in this study.

5. Results and discussion

5.1. Weber and Reynolds numbers effect on macroscopic spray structure

For the fuels and temperature-pressure conditions evaluated, the Weber number varies from 3000 to 120,000 and the Reynolds number varies from 1500 to 63,000. On a Weber number versus Reynolds number domain, six regions were selected to examine the relative importance of the inertia force, surface tension force, and viscous force; the air-to-liquid density ratio was maintained at 0.002 for this comparison. These regions are illustrated in Fig. 6 with the corresponding test conditions shown in Table 3. The viscous and surface tension forces primarily depend on fuel type and fuel temperature. The inertia force primarily depends on the injection-to-ambient pressure differential with a secondary contribution associated with the fluid viscosity. As the change in the surface tension force is considerable smaller compared to the changes in both the inertia and viscous forces, this analysis focuses on describing the influence of the inertia and viscous forces on the macroscopic spray characteristics.

As illustrated in Fig. 6, region one describes low Weber and Reynolds number conditions. This region is characteristic of small inertia forces due to low injection pressure with large viscous forces due to low fuel temperature. Together, these provide a relatively small spray momentum where a weak interaction between liquid and surrounding air is anticipated. The spray plumes illustrated exhibit a low penetration with a narrow spray plume width, consistent with Rayleigh breakup theory.

Region two describes low Weber number with moderate Reynolds number conditions. For this region, the inertia forces are low and similar to region one; resulting in low Weber numbers. The higher Reynolds number results from lower viscous force due to higher fuel temperatures. Consistent with Ref. [23], higher spray penetration is observed in this region due to the higher initial spray velocity expected as a result of lower frictional losses within the injector. The higher Reynolds number typically leads to turbulent liquid motion with an accelerated breakup process; however, the low Weber number implies a small inertia force relative to the surface tension force; providing poor breakup of the spray's liquid core.

Region three describes high Weber number and moderate Reynolds number conditions. The fuel spray in this region has relatively large inertial forces due to high injection pressures and large viscous forces due to low fuel temperatures. This combination

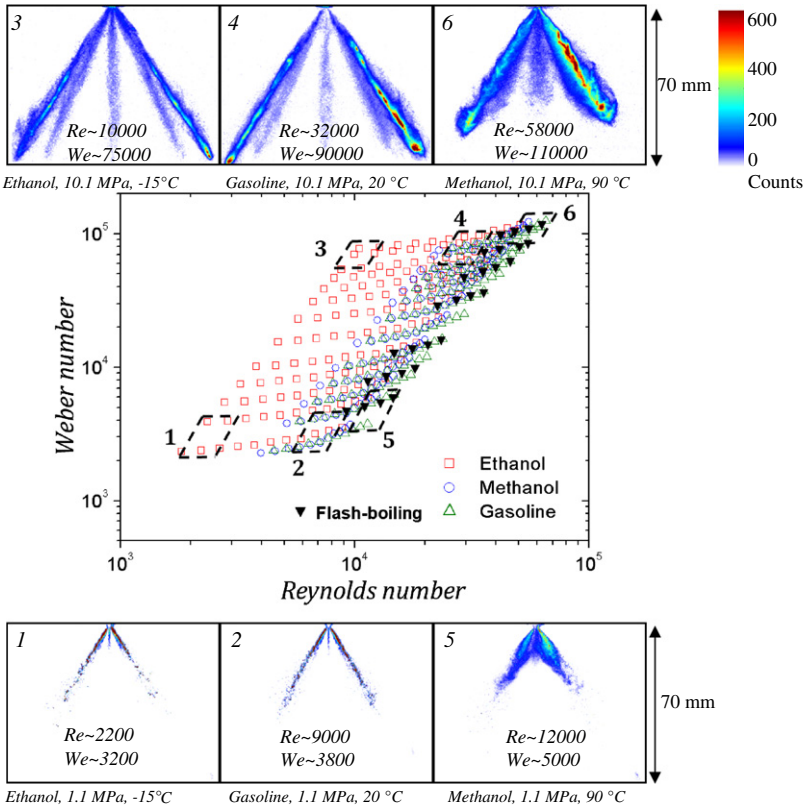

Fig. 6. Sprays at 1 ms after-start-of-injection (ASOI) from multi-hole injector in typical regions on a Weber number versus Reynolds number domain.

Table 3
Operating conditions for typical regions.

Region	We	Re	Fuel type	Injection pressure (MPa)	Fuel temp. (°C)
1	3200	2200	Ethanol	1.1	−15
2	3800	9000	Gasoline	1.1	20
3	10,000	75,000	Ethanol	10.1	−15
4	32,000	90,000	Gasoline	10.1	20
5	5000	12,000	Methanol	1.1	90
6	58,000	110,000	Methanol	10.1	90

leads to higher liquid momentum and corresponding higher spray penetration. According to spray atomization theory [1], the relatively high inertia force will accelerate the breakup process resulting in expanded spray plumes, which is consistent with the observations illustrated in Fig. 6.

Region four describes large Weber number and large Reynolds number conditions. In this region, the inertia forces are high and similar to region three; resulting in high Weber numbers. The higher Reynolds number results from lower viscous force due to higher fuel temperatures. Lower viscous forces are expected to accelerate the breakup process, increasing the spray penetration and spray–plume angle. However, only minor differences in the macroscopic spray structure between regions three and four are observed; indicating the viscous effect plays a less important role on the spray breakup compared to the inertia force.

For regions five and six, a dramatic spray transformation occurs as the ambient pressure is below the fuel saturation pressure. Under these flash-boiling conditions, the spray exhibits a significantly wider spray-cone angle, lower spray penetration, and a more uniform spray distribution compared to the non-flash-boiling case. The flash-boiling spray structure depends on the forces associated with bubble formation and expansion so the dimensionless numbers examined for the non-flash-boiling liquid spray breakup is not expected to accurately represent the flash-boiling situation. Therefore, the dimensionless analysis for examining spray structure conducted in this study focuses on non-flash-boiling sprays.

5.2. Air-to-liquid density ratio effect on macroscopic spray structure

In addition to the Reynolds and Weber numbers, the air-to-liquid density ratio (ρ_a/ρ_l) is another important dimensionless parameter that influences the macroscopic spray structure. As an example, Fig. 7 illustrates methanol sprays at one millisecond after-start-of-injection (ASOI) for air-to-liquid density ratios between 0.0008 and 0.02 with nearly constant Weber and Reynolds numbers. In this comparison, the fuel temperature is 0 °C and the fuel pressure is 10 MPa. The Weber and Reynolds numbers are near 74,000 and 25,000, respectively. The air-to-liquid density ratio ranges from 0.0008 to 0.02, corresponding to ambient pressures between 40 kPa and 1 MPa. The spray macroscopic structure is shown to exhibit a significant transformation when changing the air-to-liquid density ratio. More specifically, the spray penetration decreases with the increasing air-to-liquid density ratio. In addition, the smallest spray–plume angle is observed at an ambient pressure of 100 kPa with increasing spray–plume angle at for lower and higher ambient pressures.

Fig. 8 presents the spray penetration and spray–plume angle as a function of the air-to-liquid density ratio; covering small, moderate, and large Weber and Reynolds numbers. For all conditions, the spray penetration decreases with increasing air-to-liquid density ratio. The spray–plume angle has a minimum value at an air-to-liquid density ratio of 0.002, an ambient pressure near 100 kPa. Increasing spray–plume angle occurs when both increasing and

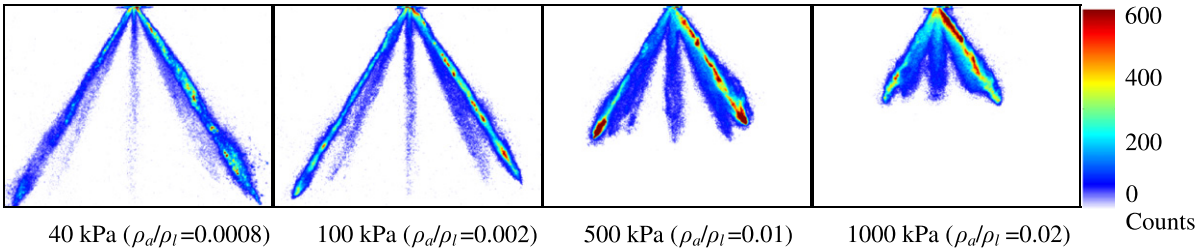

Fig. 7. Effect of air-to-liquid density ratio illustrated for a methanol spray. Spray images shown at a fuel temperature of 0 °C and fuel pressure of 10 MPa; Weber and Reynolds numbers near 74,000 and 25,000, respectively.

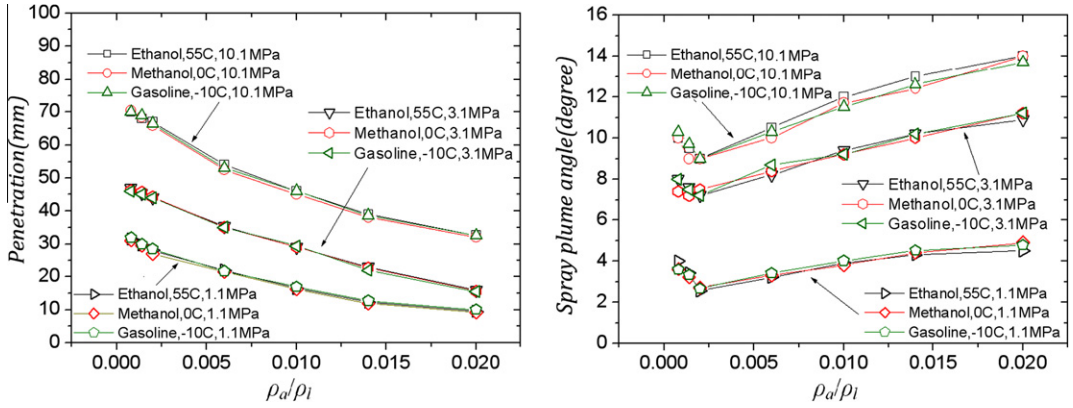

Fig. 8. Spray penetration (left) and spray–plume angle (right) for different fuels under various conditions.

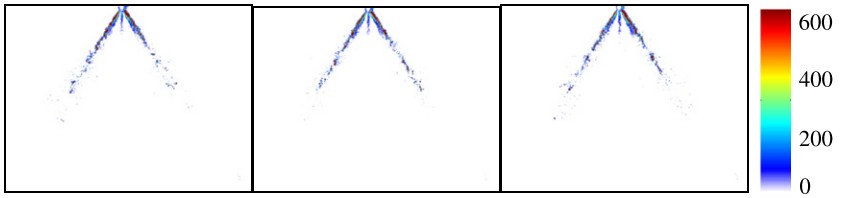

Ethanol 55°C Methanol 0°C Gasoline -15°C
Fuel pressure of 0.6 MPa and ambient pressure of 100 kPa

(a) The Weber number, Reynolds number and ρ_a/ρ_l are 2350, 3800 and 0.002, respectively

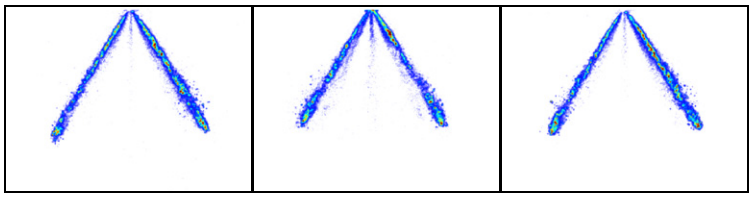

Ethanol 55°C Methanol 0°C Gasoline -15°C
Fuel pressure of 3.1 MPa and ambient pressure of 100 kPa

(b) The Weber number, Reynolds number and ρ_a/ρ_l are 20000, 13000 and 0.002, respectively

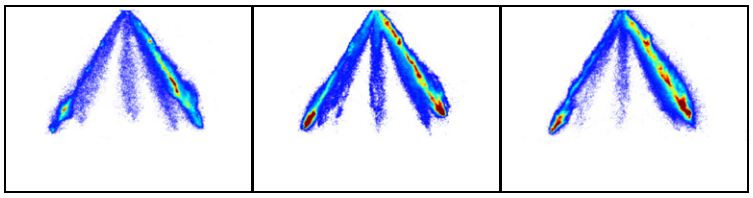

Ethanol 55°C Methanol 0°C Gasoline -15°C
Fuel pressure of 10.1 MPa and ambient pressure of 500 kPa

(c) The Weber number, Reynolds number and ρ_a/ρ_l are 77000, 23000 and 0.01, respectively

Fig. 9. Sprays have the similar magnitudes of dimensionless numbers.

decreasing ambient pressure from 100 kPa. These trends are consistent for all regions, indicating that the air-to-liquid density ratio plays different roles to affect the spray–plume angle in a pressurized environment as compared to a vacuum environment.

These observed spray–plume angle trends indicate different breakup mechanisms under the pressurized and vacuum ambient conditions. When the ambient pressure is above 100 kPa, the spray induced air entrainment is dominated by the aerodynamic breakup process which enhances the liquid fuel dispersion. At higher air-to-liquid density ratios, for example, a stronger interaction occurs between the liquid and surrounding air, leading to larger spray–plume angles. When the ambient pressure is below 100 kPa, aerodynamic force has a reduced influence on the primary atomization onset and droplets and it is not anticipated to be the dominant mechanism in the breakup process [24–26]. The motion of ligament that results from randomly directed liquid velocity fluctuation becomes more important for spray breakup and it plays a primary role to affect spray breakup. When decreasing the ambient pressure, cavitation is a potential reason to strengthen liquid fluctuation. According to the previous study [20–22], cavitation could occur under the test conditions used in this study. The level of cavitations increases when decreasing the ambient pressure. It can strengthen the motion of ligament and enhance the breakup process resulting in a larger spray–plume angle. However, the previous cavitation study [27] based on direct-injection diesel nozzles indicates that cavitation is a complex phenomenon. The previous study [28] on cavitation in gasoline direct-injection engines, which shows massive cavitation structures during needle opening, indicates that gasoline direct-injection atomization is very different from diesel direct-injection nozzle flow and breakup. These studies indicate that the further research is necessary to understand the effect of cavitation on liquid fluctuation and fuel dispersion.

5.3. Sprays with similar magnitudes of dimensionless numbers

Fig. 9 shows gasoline, methanol and ethanol sprays at one millisecond after-start-of-injection (ASOI) for three regions, representing small, moderate and large Weber and Reynolds numbers. In each region, the fuel type, fuel temperature, fuel pressure, and ambient pressure are different, but the magnitudes of Weber number, Reynolds number, and air-to-liquid density ratio are nearly constant. When maintaining these dimensionless numbers constant, a similar macroscopic spray structure is observed for the three fuels in each region. This result confirms the classical aerodynamic atomization theory based on non-dimensional analysis. A more quantitative analysis is provided in Fig. 10, where the spray penetration is shown as a function of time elapsed ASOI and spray–plume angle is provided at one millisecond ASOI. These data further demonstrate that the macroscopic spray structure is similar for gasoline, methanol, and ethanol fuels when comparing at similar Weber number, Reynolds number, and air-to-liquid density ratio.

The revealed spray similarity is due to the relationship between the spray breakup mechanism and the forces associated with the above three dimensionless numbers. Spray breakup depends on the competition among the inertia force, surface tension force, viscous force, and air resistance acting on the liquid jet surface. The Weber number, Reynolds number, and air-to-liquid density ratio quantify the competitions among these forces. Regardless of fuel type and test conditions for non-flash-boiling sprays, therefore, a

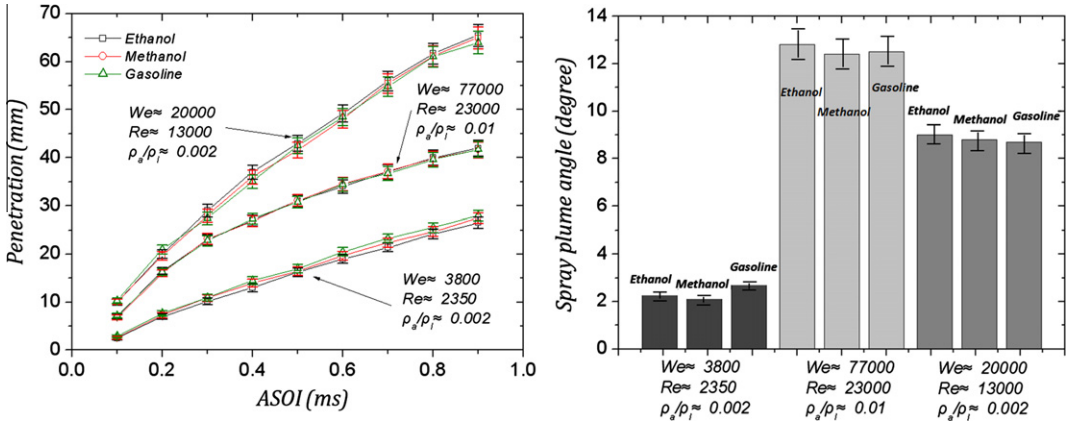

Fig. 10. Spray penetrations (left) and plume angles (right) of the sprays in Fig. 9.

similar spray breakup process and resulting spray structure is anticipated when maintaining these dimensionless parameters at similar values.

5.4. Correlations between spray macroscopic characteristics and dimensionless numbers

Fig. 11 illustrates the spray penetration and spray–plume angle versus Reynolds number, data compared at one millisecond ASOI. In general, these macroscopic spray parameters increase in a near linear fashion with increasing Reynolds number. This behavior is attributed to the viscosity change as the observation is made assuming constant injection pressure and air-to-liquid density ratio conditions. Temperature change is the primary driver for increase in Reynolds number since the change in temperature leads to decrease in viscosity. More specifically, the lower viscous fluid is ejected from the nozzle at a higher initial velocity due to lower frictional losses within the injector; increasing the inertia force and corresponding spray penetration. In the Zigan's study [13] mentioned above, there is a 3% reduced injected fuel mass mentioned for a high-viscosity fuel for a similar injector. Probably this happened also in the current study and could explain the slightly different behavior for ethanol (changed spray momentum, slightly reduced penetration). A larger spray–plume angle with increasing Reynolds number is expected to result from the lower viscosity due to a stronger interaction between the liquid and surrounding air. It is also expected to result from the strengthened nozzle inside turbulence as a result of the increased fuel temperature, according to the previous cavitation study based on two-dimensional simplified nozzles [22]. These trends and conclusions are consisted with that reported in Ref. [1] for different geometries and injection conditions. For the same test conditions, the spray penetration of ethanol is slightly smaller than that of gasoline and methanol and the differences in the penetration between gasoline and methanol is relatively small. Such small differences are also observed in the spray–plume angle among these three fuels. The injection pressure and air-to-liquid density ratio have significant effects on the spray penetration and spray–plume angle, where increase in density ratio results in larger changes in spray penetration and spray–plume angle as compared to increase in injection pressure. From the slope of the curve it is also apparent that fuel effects have smaller effects compared to injection pressure and ambient density effects, but cannot be neglected.

Fig. 12 illustrates the spray penetration and spray–plume angle versus Weber number. When comparing these data at constant air-to-liquid density ratio, strong correlations are observed for both the spray penetration and spray–plume angle as described by the following equations:

$$S \propto \mathrm{We}^{0.318} \tag{3}$$

$$\theta \propto \mathrm{We}^{0.46} \tag{4}$$

where S is spray penetration and θ is the spray–plume angle at one millisecond ASOI. These two expressions primarily describe the effect of the inertia force on spray penetration and spray–plume angle as the difference in the surface tension among all the conditions evaluated is relatively small.

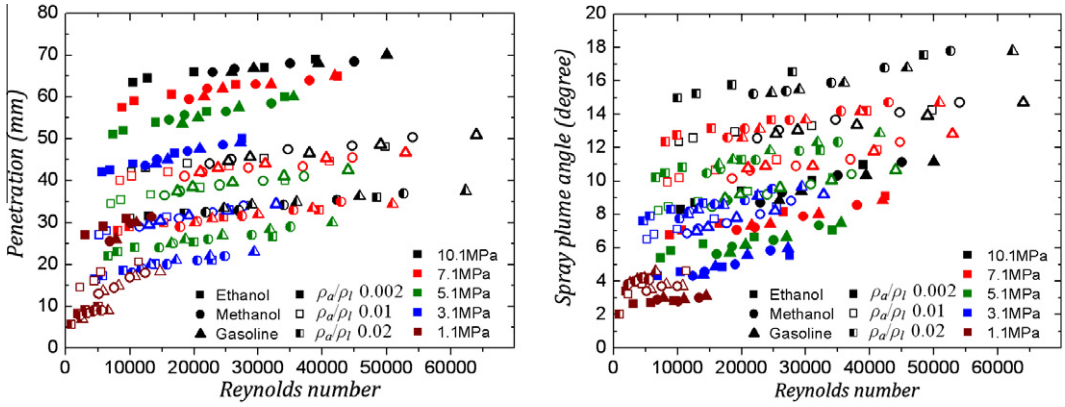

Fig. 11. Spray penetration (left) and plume angle (right) versus Reynolds number.

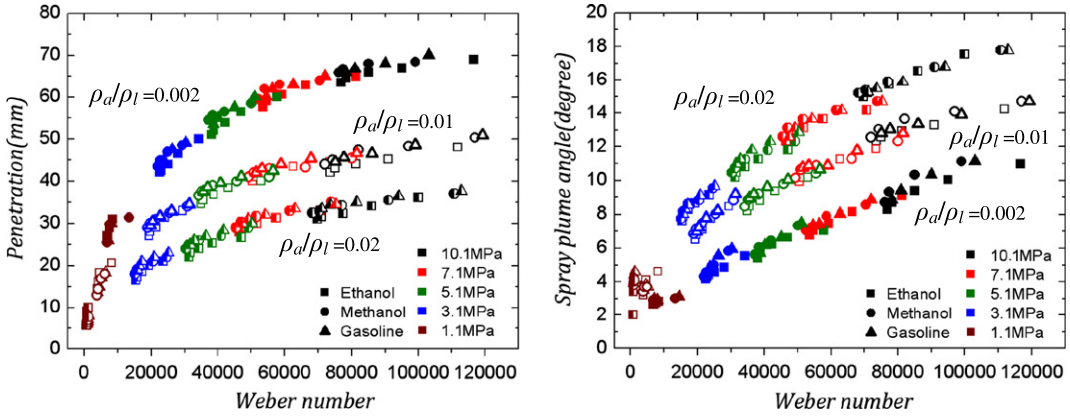

Fig. 12. Spray penetration (left) and plume angle (right) versus Weber number.

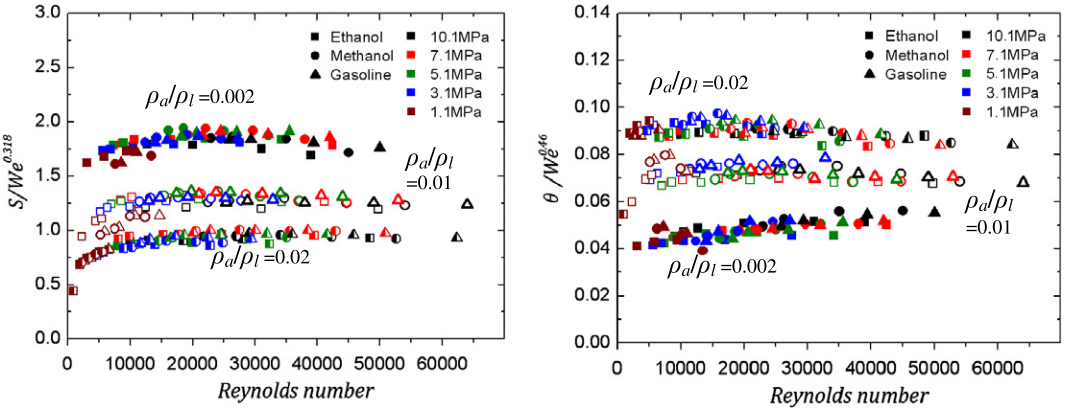

Fig. 13. $S/We^{0.318}$ (left) and $\theta/We^{0.46}$ (right) versus Reynolds number.

The expressions (3) and (4) provide a quantification of the inertia effect on spray penetration and spray–plume angle. To isolate the Weber number effect from the other dimensionless numbers, the spray penetration and the spray–plume angle are divided by expressions (3) and (4), respectively. Fig. 13 shows the correlations between the new dependent variables that represent the spray penetration and spray–plume angle compared to the Reynolds number. At each air-to-liquid density ratio, a single curve is shown that now comprehends the effect of injection pressure. Consistent with the analysis in Section 5.2, these data illustrate the dominate effect of the air-to-liquid density ratio on the spray penetration and spray–plume angle, which is provided by the following equation:

$$S \propto (\rho_a/\rho_l)^{-0.268} \tag{5}$$

$$\theta \propto (\rho_a/\rho_l)^{0.287} \tag{6}$$

Combining expressions (3)–(6), the spray penetration and spray–plume angle are represented by two new variables that comprehend the Weber number effect and the air-to-liquid density ratio effect; namely $S/We^{0.318}(\rho_a/\rho_l)^{-0.268}$ and $\theta/We^{0.46}(\rho_a/\rho_l)^{0.287}$, respectively. These new variables are plotted against the Reynolds number include all the test conditions evaluated in this study, shown in Fig. 14. These plots illustrate the quantified effect of viscous force on spray penetration and spray–plume angle. A plateau line is determined when the Reynolds number becomes larger than 12,500, indicating limited effect of the viscous forces on the spray penetration and spray–plume angle. For lower Reynolds numbers, increasing viscous force leads to reductions in the spray penetration and spray–plume angle. Therefore, the viscous effect plays a more important role on spray macroscopic characteristics for lower Reynolds number conditions; specifically when the Reynolds number is below 12,500. This agrees with the findings reported by Lai et al. [28] for the nozzle flow in the transitional flow regime where the Reynolds number is not very high.

Correlations were developed to comprehend the effects of all three dimensionless numbers on spray penetration and spray–plume angle, shown in Eqs. (7) and (8). For each spray parameter, two equations are provided as necessary to distinguish between different Reynolds number regimes.

$$\begin{cases} S = 0.076(\rho_a/\rho_l)^{-0.268} \cdot \mathrm{We}^{0.318} \cdot \mathrm{Re}^{0.152}, \mathrm{Re} < 12,500 \\ S = 0.33(\rho_a/\rho_l)^{-0.268} \cdot \mathrm{We}^{0.318}, \mathrm{Re} \geqslant 12,500 \end{cases} \tag{7}$$

$$\begin{cases} \theta = 0.12(\rho_a/\rho_l)^{0.287} \cdot \mathrm{We}^{0.46} \cdot \mathrm{Re}^{0.1}, \mathrm{Re} < 12,500 \\ \theta = 0.273(\rho_a/\rho_l)^{0.287} \cdot \mathrm{We}^{0.46}, \mathrm{Re} \geqslant 12,500 \end{cases} \tag{8}$$

As described in Section 5.2, the spray–plume angle has a minimum value at an air-to-liquid density ratio of 0.002 (ambient pressure near 100 kPa). The spray–plume angle increases with increasing air-to-liquid density ratio, where this behavior has been described within Eq. (8). However, for vacuum conditions, a modification is needed to capture the inverse behavior; namely, increasing spray–plume angle with decreasing air-to-liquid density ratio. This correction factor is determined by examining the spray–plume angle versus Weber and Reynolds numbers exclusively for vacuum conditions as shown in Fig. 15. The functional dependence of the spray–plume angle to the Weber and Reynolds number appear

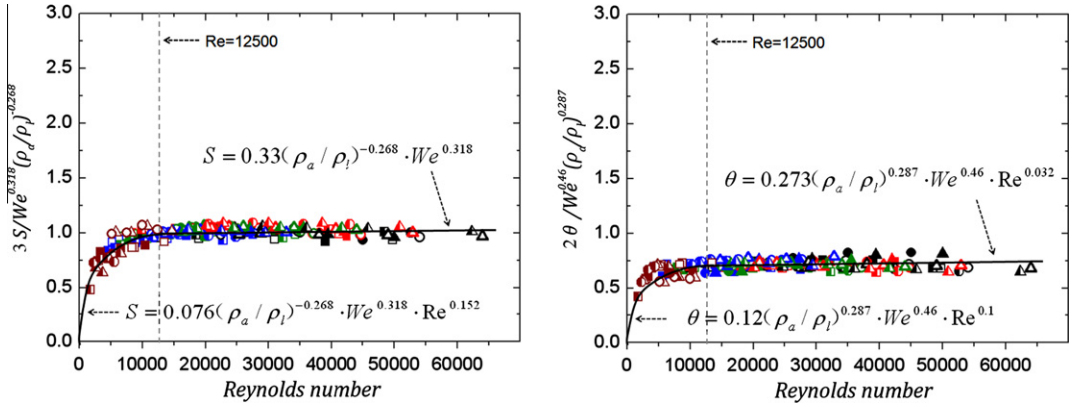

Fig. 14. Effect of dimensionless numbers on spray penetration and plume angle.

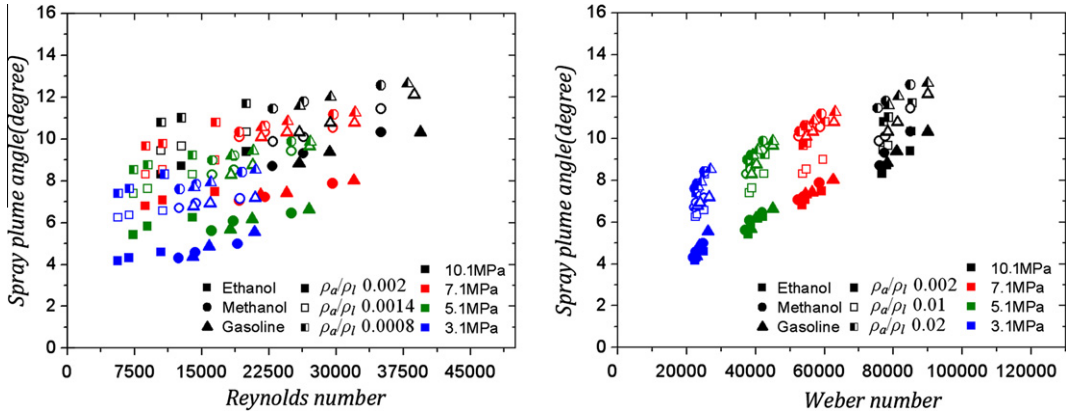

Fig. 15. Effect of dimensionless numbers on spray penetration and plume angle for vacuum conditions.

similar to that included in Eq. (8). However, the effect of air-to-liquid density ratio on the spray–plume angle under vacuum conditions requires a modified expression as provided by the following equation:

$$\theta \propto (\rho_a/\rho_l)^{-0.38} \tag{9}$$

Similar to the derivation of Eq. (8), correlations between the spray plume angle and the dimensionless numbers under vacuum conditions are provided in Eq. (10) and illustrated in the Fig. 16. Two equations are provided for the spray–plume angle to distinguish between different air-to-liquid density ratio regimes.

$$\begin{cases} \theta = 0.002(\rho_a/\rho_l)^{-0.38}\cdot \mathrm{We}^{0.46}\cdot \mathrm{Re}^{0.1}, \mathrm{Re} < 12{,}500 \\ \theta = 0.0046(\rho_a/\rho_l)^{-0.38}\cdot \mathrm{We}^{0.46}, \mathrm{Re} \geqslant 12{,}500 \end{cases} \quad \rho_a/\rho_l < 0.002 \tag{10}$$

Fig. 17 describes the calculated versus measured spray penetration and spray–plume angle; providing an assessment of the variance associated with these correlations. The maximum bandwidth is about 10% for both spray penetration and spray–plume angle data. Much of this variance is attributed to measurement uncertainty related to the image threshold value, sample size variation, fuel temperature control and fuel properties accuracies. For example, the image threshold selection approach resulted in a 20 count variation corresponding to 2% and 3% uncertainty in the spray penetration and spray–plume angle, respectively. The variation associated with a sample size is 1.5% and 2% for the spray penetration and spray–plume angle, respectively. The Reynolds number and Weber's number variance associated with fluid property uncertainty is 2%. The uncertainties associated with fuel temperature

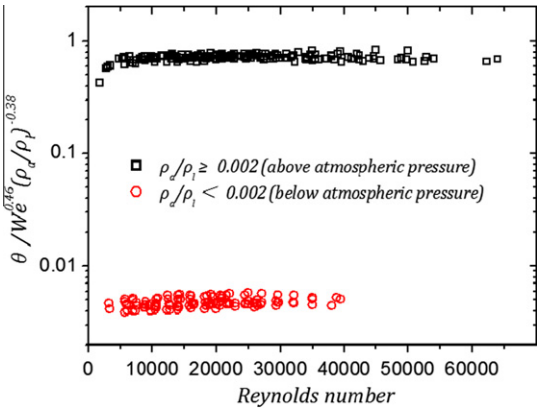

Fig. 16. Correlations for spray–plume angle at the conditions below and above atmospheric pressure.

are determined to be relatively small. These uncertainties account for the majority of the variations observed in Fig. 17, illustrating good correlations between the spray penetration, the spray–plume angle, and the dimensionless parameters examined.

5.5. Correlations for spray macroscopic characteristics

The dimensionless analysis reported in this study comprehends the effects of fuel type, fuel properties, fuel pressure, fuel temperature and ambient pressure on the non-flash-boiling sprays for a

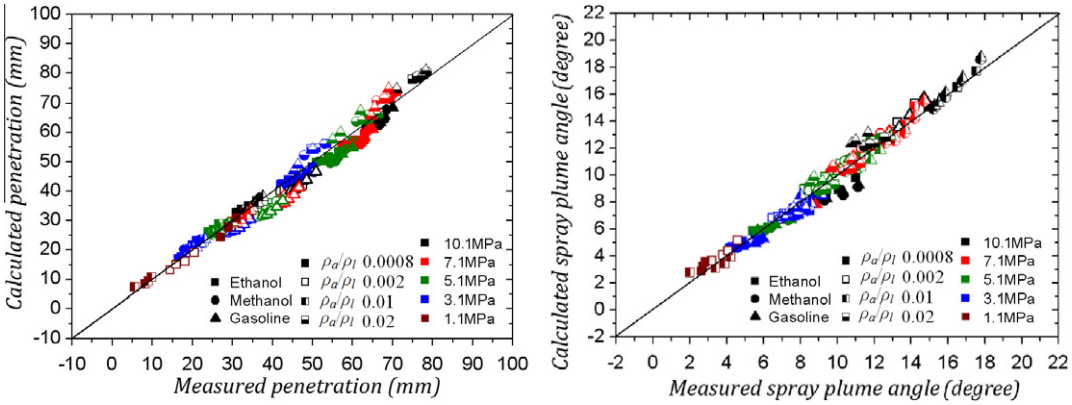

Fig. 17. Comparisons between calculated and measured spray penetration and spray–plume angle.

Table 4
Correlations for spray macroscopic characteristics.

Spray penetration and plume-angle correlations	Specifications
$S = 0.076(\rho_a/\rho_l)^{-0.268} \cdot We^{0.318} \cdot Re^{0.152}$	Re < 12,500
$S = 0.33(\rho_a/\rho_l)^{-0.268} \cdot We^{0.318}$	Re ⩾ 12,500
$\theta = 0.12(\rho_a/\rho_l)^{0.287} \cdot We^{0.46} \cdot Re^{0.1}$	Re < 12,500, $\rho_a/\rho_l \geqslant 0.002$
$\theta = 0.0273(\rho_a/\rho_l)^{0.287} \cdot We^{0.46}$	Re ⩾ 12,500, $\rho_a/\rho_l \geqslant 0.002$
$\theta = 0.002(\rho_a/\rho_l)^{-0.38} \cdot We^{0.46} \cdot Re^{0.1}$	Re < 12,500, $\rho_a/\rho_l < 0.002$
$\theta = 0.0046(\rho_a/\rho_l)^{-0.38} \cdot We^{0.46}$	Re ⩾ 12,500, $\rho_a/\rho_l < 0.002$

multi-hole nozzle. For the fuels and temperature-pressure conditions evaluated, the Weber number changes from 3000 to 120,000, the Reynolds number changes from 1500 to 63,000 and the air-to-liquid density ratio changes from 0.0008 to 0.02. This analysis yielded dimensionless correlations for spray penetration and spray–plume angle at one millisecond ASOI based on the regions of these three dimensionless numbers. The correlations do not apply in the flash-boiling conditions that the ambient pressure is below the fuel saturation pressure since the atomization mechanism of the flash-boiling spray is different with that of the non-flashing-boiling sprays [16].

The derived correlations describing the relationship between the macroscopic spray characteristics at one millisecond ASOI and dimensionless numbers are summarized in Table 4. These correlations quantify the effects of primary forces on spray penetration and spray–plume angle for a non-flash-boiling direct-injection multi-hole spray. A strong correlation is observed between these two spray parameters and Weber number, which is attributed to the inertia effect as the surface tension effect is negligible for the conditions evaluated in this study. The Reynolds number contribution primarily reflects the viscous effect on spray. When the Reynolds number is larger than 12,500, its influence on the spray penetration and spray–plume angle are reduced. The Reynolds number contribution becomes increasingly important as the Reynolds number decreases below 12,500, due to the augmented viscous effect. The air-to-liquid density ratio captures the drag force effect, where the reduced spray penetration occurs with increasing ambient density. The spray–plume angle has a minimum value at an air-to-liquid density ratio of 0.002. The spray–plume angle increases with the increasing air-to-liquid density ratio when the ambient pressure is above 100 kPa. The spray–plume angle also increases with decreasing air-to-liquid density ratio when the ambient pressure is below 100 kPa. As a result, for the non-flash-boiling multi-hole sprays in this study, the Weber number and air-to-liquid density ratio have much more profound effect on the spray penetration and spray–plume angle compared to the Reynolds number contribution. The inertia force and air drag force are more important factors compared to the viscous force and surface tension force. These formulations are different from classical formulations mentioned above, since they could be used to generate generic spray models which express the physical mechanism explicitly, independent of the test conditions and fuel type.

6. Conclusions

Dimensionless analysis was applied to investigate the macroscopic characteristics of SIDI multi-hole sprays. Weber number, Reynolds number and air-to-liquid density ratio were used to represent the primary effects on spray. Spray images was generated using Mie-scattering technique. The experiments were carried out for gasoline, methanol and ethanol fuels over a broad range of conditions found in a today's SIDI engine, ensuring the dimensionless numbers cover a relatively large domain. For the fuels and temperature-pressure conditions evaluated, the Weber number varies from 3000 to 120,000, the Reynolds number varies from 1500 to 63,000, and the air-to-liquid density ratio varies from 0.0008 to 0.02. The correlations between these dimensionless numbers and spray penetration and spray–plume angle provide a fundamental understanding of physical characteristics. The results yield formulations for spray penetration and spray–plume angle at one millisecond ASOI. The formulations do not apply in the flash-boiling conditions that the ambient pressure is below the fuel saturation pressure. The conclusions are as follows:

(1) Spray characteristics are primarily dependent on the competition among the four major forces acting on a liquid jet; the inertia force, the viscous force, the surface tension force and the air drag force, which can be represented by three dimensionless numbers, Weber number, Reynolds number, and the air-to-liquid density ratio.
(2) Sprays with similar magnitudes of Weber number, Reynolds number and air-to-liquid density ratio have similar structure and characteristics.
(3) The spray penetration decreases monotonically with the increasing air-to-liquid density ratio. However, the spray–plume angle increases with the increasing air-to-liquid density ratio when the ambient pressure is above the atmospheric pressure, and increases with decreasing air-to-liquid density ratio when the ambient pressure is below the atmospheric pressure. These opposite trends indicate different breakup mechanisms under the pressurized and vacuum ambient conditions.
(4) Strong correlations between the macroscopic spray structure (spray penetration and spray–plume angle) and Weber num-

ber are observed, which primarily describes the importance of the inertia effect as surface tension effect was relatively small for the given test conditions.

(5) When the Reynolds number is above 12,500, the effect of inertia force is significantly greater than that of viscous force; the Reynolds number effect on spray penetration and spray–plume angle are negligible. When Reynolds number is below 12,500, the viscous effect plays a more important role, especially for Reynolds numbers below 3000.

(6) For this investigation, the Weber number and air-to-liquid density ratio have much more profound effect on the spray penetration and spray–plume angle compared to the Reynolds number contribution. The inertia force and air drag force are more important factors compared to the viscous force and surface tension force.

(7) The good correlations between these three dimensionless numbers and spray macroscopic characteristics have yielded a set of general formulations. These formulations provide important insight into the spray breakup and atomization processes, and could be used to generate generic spray models which express the physical mechanism explicitly, independent of the test conditions and fuel type.

The dimensionless analysis reported in this study comprehends the effects of fuel type, fuel properties, fuel pressure, fuel temperature and ambient pressure for a multi-hole nozzle. It is necessary to notice that the correlations yielded in this study do not consider the effect of geometrical nozzle configuration. Further investigation will be carried out for different multi-hole designs to yield more general dimensionless correlations. Therefore, when applying the correlations to other multi-hole designs, caution should be taken until further validated and the spray penetration and plume angle correlations can be used to indicate the relative values. On the other hand, no temporal information is provided so that only the quasi-stationary injection phase at complete needle opening is considered (1 ms ASOI). But also throttling effects for needle-opening and closing may be relevant, when the Re and We numbers are much smaller (and cavitation may be more relevant).

Acknowledgments

The research was carried out at National Engineering Laboratory for Automotive Electronic Control Technology in Shanghai Jiao Tong University, and sponsored by General Motors Company and National Natural Science Foundation of China (Nos. 51076093/E060702 and 51076090/E060404).

References

[1] A.H. Lefebvre, Atomization and Sprays, Taylor Francis, New York, 1989.
[2] H. Hiroyasu, M. Arai, Structures of Fuel Sprays in Diesel Engines, SAE Paper 900475, 1990.
[3] H. Hiroyasu, Spray breakup mechanism from the hole-type nozzle and its applications, Atom. Sprays 10 (2000) 511–527.
[4] X. Wang, J. Gao, D. Jiang, Z. Huang, W. Chen, Spray characteristics of high-pressure swirl injector fueled with methanol and ethanol, Energy Fuels 19 (2005) 2394–2401.
[5] P.G. Aleiferis, J. Serras-Pereira, Z.V. Romunde, J. Caine, M. Wirth, Mechanisms of spray formation and combustion from a multi-hole injector with E85 and gasoline, Combust. Flame 157 (2010) 735–756.
[6] K. Lee, R.D. Reitz, Investigation of spray characteristics from a low-pressure common rail injector for use in a homogeneous charge compression ignition engine, Meas. Sci. Technol. 15 (2004) 509–519.
[7] S. Moon, E. Abo-Serie, C. Bae, Air flow and pressure inside a pressure-swirl spray and their effects on spray development, Exp. Therm. Fluid Sci. 33 (2009) 222–231.
[8] M.R. Halder, S.K. Dash, S.K. Som, A numerical and experimental investigation on the coefficients of discharge and the spray cone angle of a solid cone swirl nozzle, Exp. Therm. Fluid Sci. 28 (2004) 297–305.
[9] J. Naber, D.L. Siebers, Effects of Gas Density and Vaporization on Penetration and Dispersion of Diesel Sprays, SAE Paper 960034, 1996.
[10] J.M. Desantes, R. Payri, F.J. Salvador, A. Gil, Development and validation of a theoretical model for diesel spray penetration, Fuel 85 (2006) 910–917.
[11] S. Park, H. Suh, C. Lee, Effect of bioethanol–biodiesel blending ratio on fuel spray behavior and atomization characteristics, Energy Fuels 23 (2009) 4092–4098.
[12] L. Zigan, I. Schmitz, A. Flügel, M. Wensing, A. Leipertz, Structure of evaporating single- and multi-component fuel sprays for 2nd generation gasoline direct injection, Fuel 90 (2011) 348–363.
[13] L. Zigan, I. Schmitz, A. Flügel, T. Knorsch, M. Wensing, A. Leipertz, Effect of fuel properties on spray breakup and evaporation studied for a multi-hole direct injection spark ignition (DISI) injector, Energy Fuels 24 (2010) 4341–4350.
[14] C. Dumouchel, On the experimental investigation on primary atomization of liquid streams, Exp. Fluids 45 (2008) 371–422.
[15] Z. Liu, R.D. Reitz, An analysis of the distortion and breakup mechanisms of high speed liquid drops, Int. J. Multiph. Flow 23 (1997) 631–650.
[16] W. Zeng, M. Xu, G. Zhang, Y. Zhang, D.J. Cleary, Atomization and vaporization for flash-boiling multi-hole sprays with alcohol fuels, Fuel 95 (2012) 287–297.
[17] E. Sher, T. Bar-Kohany, A. Rashkovan, Flash-boiling atomization, Prog. Energy Combust. Sci. 24 (2008) 417–439.
[18] J. Lee, R. Madablushi, S. Fotache, S. Gopalakrishnan, D.P. Schmidt, Flashing flow of superheated jet fuel, Proc. Combust. Inst. 32 (2009) 3215–3222.
[19] B. Zhu, M. Xu, Y. Zhang, G. Zhang, Physical properties of gasoline-alcohol blends and their influences on spray characteristics from a low-pressure DI injector, in: Proceedings of the 14th Asia Annual Conference on Liquid Atomization and Spray Systems, Jeju, Korea, 2010.
[20] J. Serras-Pereiza, Z. van Romunde, P.G. Aleiferis, D. Richardson, S. Wallace, R.F. Cracknell, Cavitation, primary break-up and flash boiling of gasoline, iso-octane and *n*-pentane with a real-size optical direct-injection nozzle, Fuel 89 (2010) 2592–2607.
[21] P.G. Aleiferis, J. Serras-Pereira, A. Augoye, T.J. Davies, R.F. Cranknell, D. Richardson, Effect of fuel temperature on in-nozzle cavitation and spray formation of liquid hydrocarbons and alcohols from a real-size optical injector for direct-injection spark-ignition engines, Int. J. Heat Mass Tran. 53 (2010) 4588–4606.
[22] A. Sou, S. Hosokawa, A. Tomiyana, Effects of cavitation in a nozzle on liquid jet atomization, Int. J. Heat Mass Tran. 50 (2007) 3575–3582.
[23] W. Zeng, M.Xu, M. Zhang, Y. Zhang, D.J. Cleary, Characterization of Methanol and Ethanol Sprays from Different DI Injectors by Using Mie-scattering and Laser Induced Fluorescence at Potential Engine Cold-start Conditions, SAE Paper 2010-01-0602, 2010.
[24] P.K. Wu, L.K. Tseng, G.M. Faeth, Primary breakup in gas/liquid mixing layers for turbulent liquids, Atom. Sprays 2 (1992) 295–317.
[25] T.E. Parker, L.R. Raimaldi, W.T. Rawlins, A comparative study of room-temperature and combustion fuel sprays near the injector tip using infrared laser diagnostics, Atom. Sprays 8 (1998) 565–600.
[26] G.M. Faeth, L.P. Hsiang, P.K. Wu, Structure and break-up properties of sprays, Int. J. Multiph. Flow 21 (1995) 99–127.
[27] A. Andriotis, M. Gavaises, C. Arcoumanis, Vortex flow and cavitation in diesel injector nozzles, J. Fluid Mech. 610 (2008) 195–215.
[28] M.C. Lai, Y. Zheng, A. Matsumoto, J. Wang, X. Zhang, S. Moon, J. Gao, K. Fezzaa, L. Zigan, I. Schmitz, M. Wensing, A. Leipertz, Characterisation of Internal Flow and Spray of Multihole DI Gasoline Spray using XRay Imaging and CFD, SAE Paper 2011-01-1881, 2011.